

Robust Quantum Control for the Manipulation of Solid-State Spins

Yifan Zhang,^{1,2,§} Hao Wu^{1,2,§} Xiaodong Yang,^{3,4,5,§} Tianyu Xie,^{6,7} Ye-Xin Wang,⁸ Chang Liu,^{1,2} Qing Zhao,^{1,2,*} Jiyang Ma,^{1,2,*} Jun Li,^{3,4,5,†} and Bo Zhang^{1,2,‡}

¹*Center for Quantum Technology Research and Key Laboratory of Advanced Optoelectronic Quantum Architecture and Measurements (MOE), School of Physics, Beijing Institute of Technology, Beijing 100081, China*

²*Beijing Academy of Quantum Information Sciences, Beijing 100193, China*

³*Shenzhen Institute for Quantum Science and Engineering, Southern University of Science and Technology, Shenzhen 518055, China*

⁴*International Quantum Academy, Shenzhen 518048, China*

⁵*Guangdong Provincial Key Laboratory of Quantum Science and Engineering, Southern University of Science and Technology, Shenzhen 518055, China*

⁶*CAS Key Laboratory of Microscale Magnetic Resonance and School of Physical Sciences, University of Science and Technology of China, Hefei 230026, China*

⁷*CAS Center for Excellence in Quantum Information and Quantum Physics, University of Science and Technology of China, Hefei 230026, China*

⁸*Spin-X Institute, School of Chemistry and Chemical Engineering, State Key Laboratory of Luminescent Materials and Devices, Guangdong-Hong Kong-Macao Joint Laboratory of Optoelectronic and Magnetic Functional Materials, South China University of Technology, Guangzhou 510641, China*

(Received 4 May 2022; revised 22 October 2022; accepted 15 February 2023; published 21 March 2023)

Robust and high-fidelity control of electron spins in solids is the cornerstone for facilitating applications of solid-state spins in quantum information processing and quantum sensing. However, precise control of spin systems is always challenging due to the presence of various noises originating from the thermal environment and control fields. Here, noise-resilient quantum gates, designed with robust optimal control (ROC) algorithms, are demonstrated experimentally with nitrogen-vacancy centers in diamond to realize tailored robustness against detunings and Rabi errors simultaneously. In the presence of both 10% off-resonance detuning and 10% deviation of a Rabi frequency, we achieve an average single-qubit gate fidelity of up to 99.89%. Our experiments also show that, ROC-based multipulse quantum sensing sequences can suppress spurious responses resulting from finite widths and imperfections of microwave pulses, which provides an efficient strategy for enhancing the performance of existing multipulse quantum sensing sequences.

DOI: 10.1103/PhysRevApplied.19.034068

I. INTRODUCTION

Quantum optimal control (QOC) provides a powerful strategy to improve process performance in quantum technologies by designing efficient control fields against pulse errors in quantum operations. Fundamental quantum operations, such as state preparations, noise suppression, and high-fidelity quantum gates [1,2], play significant roles in magnetic resonance spectroscopy and imaging [3], quantum information processing [4–6], and quantum sensing [7–12], which may benefit from recent advances of QOC [13].

To date, various methods have been developed to achieve high-fidelity operations such as composite pulses [14]. However, for conventional composite pulses, such as broadband number 1 pulse (known as BB1 [15]) and compensation for off-resonance errors with a pulse sequence (known as CORPSE [16]), they are robust against a single type of pulse errors; for concatenated composite pulses, such as BB1inC [17], although it can simultaneously correct various types of existing errors but at the price of large pulse widths.

In this work, by exploiting robust optimal control (ROC) algorithms [18,19] in pulse-sequence designs, we experimentally demonstrate ROC as a simple, effective, and hardware-friendly approach of quantum optimal control for realizing high-fidelity quantum gates and extensive robustness to multiple pulse errors. The ROC approach enables suppression of pulse errors to the second order

*mjj@bit.edu.cn

†lij3@sustech.edu.cn

‡bozhang_quantum@bit.edu.cn

§These authors contributed equally.

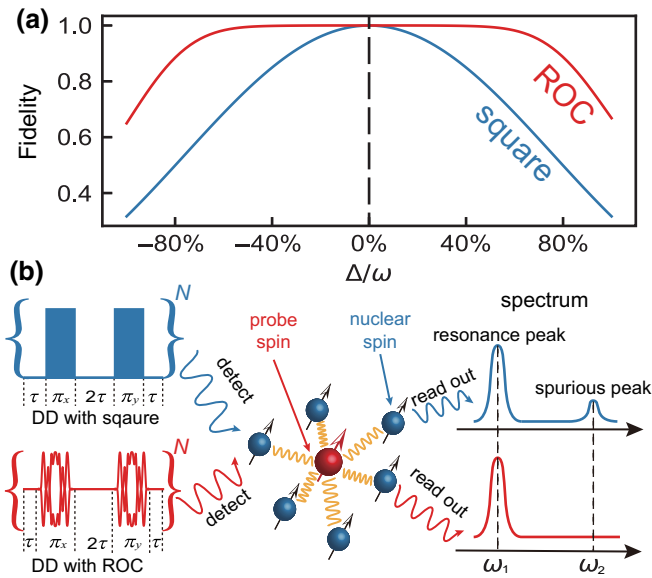


FIG. 1. (a) Comparison of the robustness of square and ROC pulses against pulse imperfections. The blue (red) curve is simulated fidelities of square (ROC) π pulses with detunings of MW frequency ranging from $-\Omega$ to Ω , where Ω is the Rabi frequency. (b) Schematic of detecting and manipulating weakly coupled spins with dynamical decoupling (DD) sequences. Typical square-based and ROC-based DD sequences are shown in the left part. The spectra derived from the two DD sequences are shown in the right part. The real peak at ω_1 results from surrounded nuclear spins and the spurious peak at ω_2 results from the finite pulse length width and imperfections of square pulses whereas the ROC pulses strongly suppress spurious peaks.

and provides an all-round robust region for quantum operations compared with conventional approaches, as shown in Fig. 1(a). Additionally, combining dynamical decoupling (DD) sequences with ROC, spurious peaks arising from finite pulse widths and pulse imperfections can be suppressed, as shown in Fig. 1(b).

II. QUANTIFICATION OF SYSTEM ERRORS

ROC-based high-fidelity single-qubit gates are demonstrated on a single electron spin of a negatively charged nitrogen-vacancy (N-V) defect center in diamond. The ground state of the N-V center ($S = 1$) is an electron-spin triplet state with three sublevels $|m_s = 0\rangle$ and $|m_s = \pm 1\rangle$. A bias magnetic field of $B_0 = 510$ Gauss is applied to separate the degenerate levels. The spin states $|m_s = 0\rangle$ and $|m_s = -1\rangle$ are encoded as a qubit. The general Hamiltonian of the N-V center with microwave (MW) control is

$$\begin{aligned} H_{\text{N-V}} = & (\Delta + \delta_0)S_z \\ & + (\Omega + \delta_1)(\cos(\phi + \delta_\phi)S_x + \sin(\phi + \delta_\phi)S_y), \end{aligned} \quad (1)$$

where Δ is the detuning of MW control relative to the N-V center's resonance frequency, which we take as constant here, Ω and ϕ are the Rabi frequency and phase of MW pulse, respectively. The corresponding errors resulting in gate errors are δ_0 , δ_1 , and δ_ϕ , respectively. δ_0 represents static field errors arising from the Overhauser field, magnetic fluctuations, and unstable MW frequencies. δ_1 consists of two parts, namely, (i) MW-amplitude errors mainly arising from static fluctuations of MW powers; (ii) errors of random noise caused by fluctuations of temperature and instability of radiation efficiency of coplanar waveguides. The phase error δ_ϕ is attributed to imperfect MW generation. After optimizing the microwave circuits in Appendix A, we quantify the errors resulting from the fluctuations of the experimental parameters. We assume that the timescale of δ_0 and δ_1 were much longer than that of the single experiment, so the two errors are taken as quasistatic random contrasts. The distribution of δ_0 is measured by free induction decay (FID) experiments with a pulse sequence in the form of $R_x(\pi/2) - \tau - R_x(\pi/2)$, in which $R_x(\pi/2)$ was a rotation around x axis by an angle $\pi/2$ under the rotating frame and τ is the free-evolution time. As shown in Fig. 2(a), oscillatory FID signals are observed with the detuning of MW frequency $\Delta = 2\pi \times 2$ MHz. We assume that δ_0 satisfies a Gaussian distribution, so the probability distribution function is $f_0(\delta_0) = 1/\sigma\sqrt{2\pi}e^{-\delta_0^2/2\sigma^2}$, where σ stands for the standard

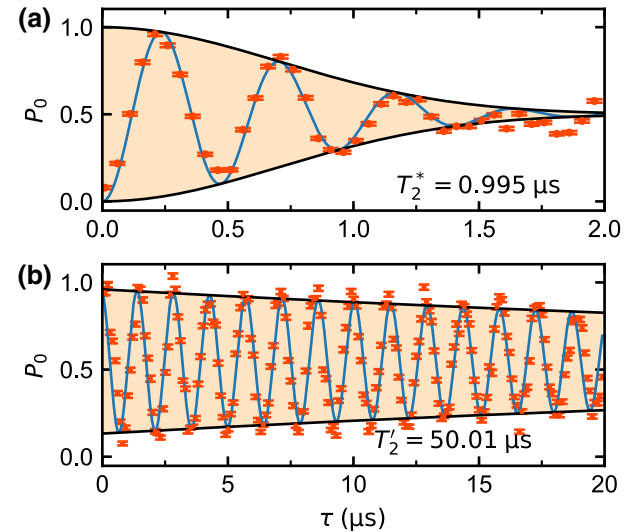


FIG. 2. Characterization of the noises in experiments. (a) Results of the FID experiment, with corresponding pulse sequence in the form of $\pi/2 - \tau - \pi/2$. Experimental data is shown as orange circles and the blue solid line is the fit of the data with $f_0(\delta_0)$. The decay time of FID signal is $T_2^* = 0.99(4)$ μ s. (b) Results of Rabi experiment. The increment of MW pulse length is set to be 100 ns. The experimental data is fit with function $f_1(\delta_1)$ (blue line). The decay time is 50(14) μ s. Error bars on the data points are standard deviations from the mean.

deviation of the distribution. The statistical probability of preserving the final state $|m_s = 0\rangle$ is

$$\begin{aligned} P &= \int_{-\infty}^{\infty} f(\delta_0) P_{\text{single}} d\delta_0 \\ &= \frac{1}{2} - \frac{1}{2} e^{-(t/T_2^*)^2} \cos(2\pi \Delta t), \end{aligned} \quad (2)$$

where $P_{\text{single}} = \frac{1}{2} - \frac{1}{2} \cos(2\pi(\Delta + \delta_0)t)$ is the probability of state $|m_s = 0\rangle$ in a single experiment, $T_2^* = 1/(\sqrt{2}\pi\sigma)$ is the decay time of FID signals. The fitting results shown in Fig. 2(a) (the blue curve) illustrated that $\sigma = 0.226(2)$ MHz and $T_2^* = 0.99(4)$ μ s. The error of Rabi frequency δ_1 is quantified via Rabi experiments where δ_1 satisfies a Lorentzian distribution of $f_1(\delta_1) = \gamma/(\pi(\delta_1^2 + \gamma^2))$, and γ stands for the half-width at half-maximum of the distribution and is inversely proportional to the decay time T_2 . The results of Rabi experiment are shown in Fig. 2(b). In order to quantify the MW field noise, we adjust the length of MW pulses from 10 ns to 20 μ s with an increment of 100 ns. The best fitting result [blue curve in Fig. 2(b)] is achieved with $T_2' = 50(14)$ μ s.

III. HIGH-FIDELITY QUANTUM GATES

After optimizing the microwave circuits and quantifying errors, we demonstrate high-fidelity single-qubit gates implementing four types of pulses, which are square, BB1, CORPSE, and ROC pulses. The pulse shapes are schematically depicted in Appendix B. Among different types of pulses, square pulses are widely used in quantum control protocols but are not sufficiently robust to detunings and Rabi errors. CORPSE and BB1 are both composite pulses; the former normally resists detunings whereas the latter is robust against Rabi errors. ROC pulses, as shaped pulses [19], can enhance robustness of quantum control against both detunings and Rabi errors. The procedure of generating a ROC pulse is described in Appendix D, Fig. 10. To quantify the fidelity of a quantum gate, we use the Clifford-based randomized benchmarking (RB) method [20–22]. A N-V electron spin is initialized to the ground state with a 532-nm laser pulse, followed by a predetermined sequence of randomized Clifford gates. Each Clifford gate is chosen randomly from the Clifford group [20], which is a set of rotations that evenly samples the Hilbert space. For single qubits, the Clifford gates comprise π , $\pi/2$, and $2\pi/3$ rotations (see Appendix E, Table II). After applying m random Clifford gates, a unique recovery Clifford gate is applied to invert the sequence. The sequence fidelity is defined as the probability of preserving the final state $|m_s = 0\rangle$. By averaging the experimental sequence fidelities over different sequences, the resulted fidelity, F_{seq} is fitted with

$$F_{\text{seq}} = \frac{1}{2} p^m + \frac{1}{2}, \quad (3)$$

where p is the sequence decay and the average fidelity per Clifford gate is given by $F_c = 1 - (1-p)/2$ [20].

To verify that ROC pulses are robust against detunings and Rabi errors, we demonstrate RB experiments based on the four different types of pulse shapes with various detunings and Rabi errors. The ranges of detunings are $\pm 2\pi \times 2$ MHz for square, $\pm 2\pi \times 4$ MHz for CORPSE and BB1, and $\pm 2\pi \times 5$ MHz for ROC, respectively. The ranges of Rabi errors are $\pm 20\%$ of Rabi frequency for square, $\pm 40\%$ for CORPSE and BB1, and $\pm 50\%$ for ROC. Each RB sequence consisted of ten Clifford gates and the sequence fidelities are calculated by averaging over 20 different sequences. Variations of the average fidelity per Clifford gate with respect to different detunings and Rabi errors are shown in Fig. 3(a), which agree with the theoretical fidelity landscapes well [see Fig. 3(b)]. It is clear that the robustness of square pulses is the worst. Meanwhile, CORPSE and BB1 reveal only selective robustness against detunings and Rabi errors, respectively. The best performance is achieved with the ROC pulses: a large flat central area with the fidelity greater than 0.99 covers the error range of $\pm 2\pi \times 3$ MHz detunings and $\pm 30\%$ Rabi frequency deviation.

IV. RANDOMIZED BENCHMARKING

We further demonstrate RB experiments with three types of pulses (square, BB1, and ROC pulses) under resonant and off-resonance conditions (see Fig. 4). The measured sequence fidelity is averaged over 50 different sequences. Under the resonant condition, the average fidelity per Clifford gate is 0.99918(5) for square, 0.99941(5) for BB1, and 0.99941(4) for ROC, respectively, showing no advantages of ROC, while under the off-resonance condition in which detunings and Rabi errors are both set to be -10% of Ω , the highest fidelity of 0.99891(9) is achieved when ROC pulses are applied.

V. DETECTION OF NUCLEAR SPINS

The ROC algorithm is applied for improving dynamical decoupling sequences in the task of detecting weakly coupled nuclear spins. Nuclear spins exist naturally in abundance in diamonds functioning as additional quantum resources [23,24]. A prerequisite to exploit nuclear spins' quantum properties is to detect and characterize the nuclear spins, which can be realized by utilizing the electron spins [25]. The Hamiltonian of the N-V spin system under the rotating frame is given by [25]

$$H = \underbrace{\Omega(x(t)S_x + y(t)S_y)}_{H_C} + \underbrace{a_{\parallel}S_zI_z + a_{\perp}S_zI_x + \omega_l I_z}_{H_{\text{free}}}, \quad (4)$$

where H_C and H_{free} are the Hamiltonians of control fields and free evolution, respectively. $x(t)$ and $y(t)$ are amplitude modulations of MW pulses, $a_{\parallel}(a_{\perp})$ represents the parallel

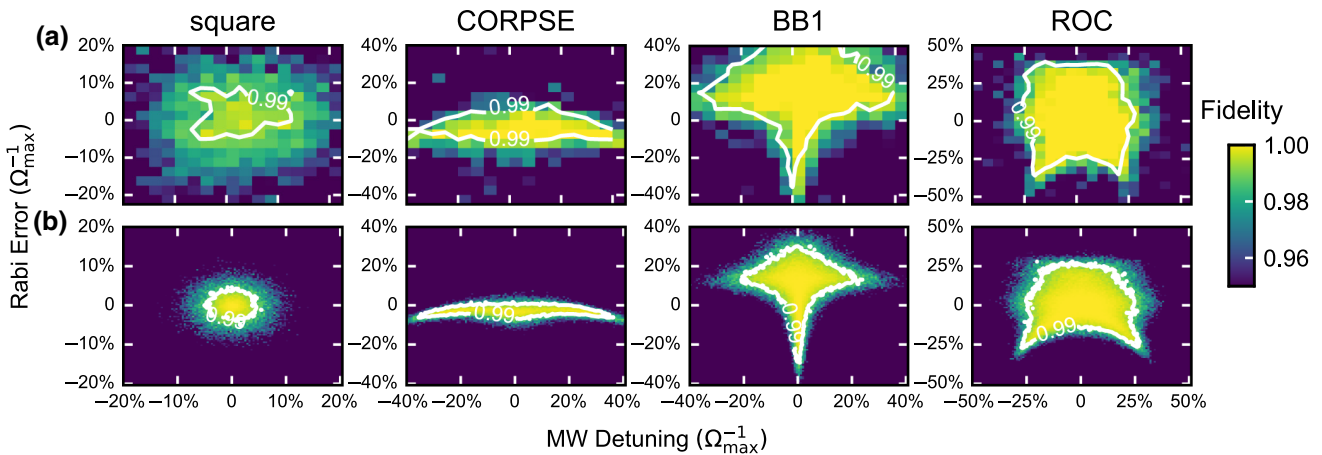


FIG. 3. Comparison of average fidelities obtained with four types of π pulses. From left to right are square, CORPSE, BB1, and ROC pulses, respectively. Measured (a) and simulated (b) average fidelity per Clifford gate obtained by RB experiments. Each fidelity is quantified with Eq. (3). The resulting sequence fidelities are averaged over 20 different sequences and the number of Clifford gate is set to 10. White lines are contour lines at a fidelity of 0.99. The ranges of detunings and Rabi errors correspond to $\pm 20\%$ of the Rabi frequency for square, $\pm 40\%$ for CORPSE and BB1, and $\pm 50\%$ for ROC.

(transverse) component of hyperfine coupling strength ω_h , and ω_l is the Larmor frequency of nuclear spins, S_x , S_y , and S_z are electron-spin operators, I_x and I_z are nuclear-spin operators. The Hamiltonian of free evolution can be reformed as

$$H_{\text{free}} = |0\rangle\langle 0| \omega_l I_z + |1\rangle\langle 1| [(\omega_l + a_{\parallel})I_z + a_{\perp}I_x], \quad (5)$$

where $|0\rangle$ ($|1\rangle$) is the electron-spin state of $|m_s = 0\rangle$ ($|m_s = -1\rangle$). It is clear that nuclear spin evolves conditionally according to the electron-spin state. Since we perform

the experiment at $B_0 = 510$ Gauss, under the approximation that $\omega_l \gg \omega_h$, the effective Larmor frequency of nuclear spins is $\omega_0 = \omega_l + a_{\parallel}/2$. Thus the effects of the surrounding nuclear-spin-bath can be considered as an ac signal whose frequency is ω_0 and amplitude is proportional to a_{\perp} acting on the electron spin [25].

By applying DD sequences (with a basic unit in the form of $\tau - \pi - 2\tau - \pi - \tau$) on the electron spin, a resonance peak indicating the coupling between the N-V electron spin and the nuclear spin should occur when the interpulse delay $2\tau = k\pi/\omega_0$ (k is odd). However, in realistic experimental implementation, each π pulse has a finite width and

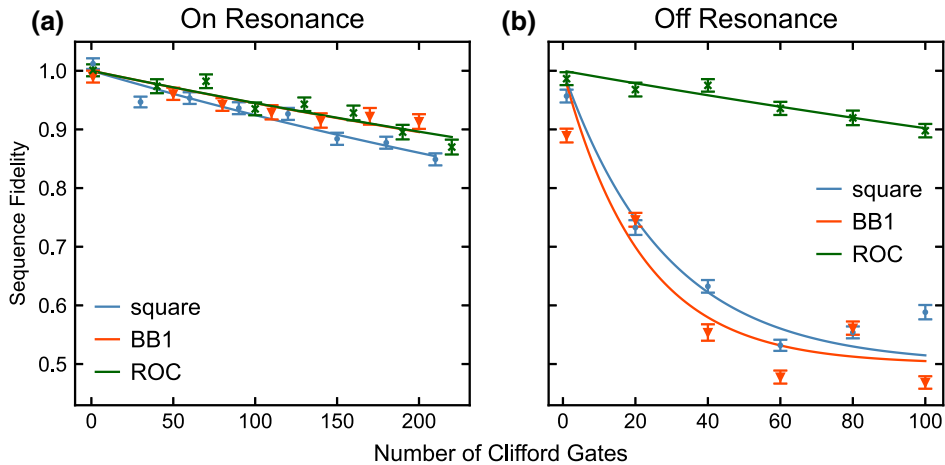


FIG. 4. (a) Results of resonant randomized benchmarking for a single qubit. Data points represent average fidelities of the final states obtained from each of the individual sequences of gates. The error bars are standard deviations from the mean. Solid lines are fit to experimental data using Eq. (3). The averaged π -pulse fidelities of square, BB1, and ROC pulses are 0.99918(5), 0.99941(5), and 0.99941(4), respectively. (b) Results of off-resonance randomized benchmarking. Both MW detunings and Rabi errors are -10% of Ω , with $\Omega = 2\pi \times 10$ MHz. The average gate fidelities of square, BB1, and ROC pulses are 0.982(2), 0.977(5), and 0.99891(9), respectively.

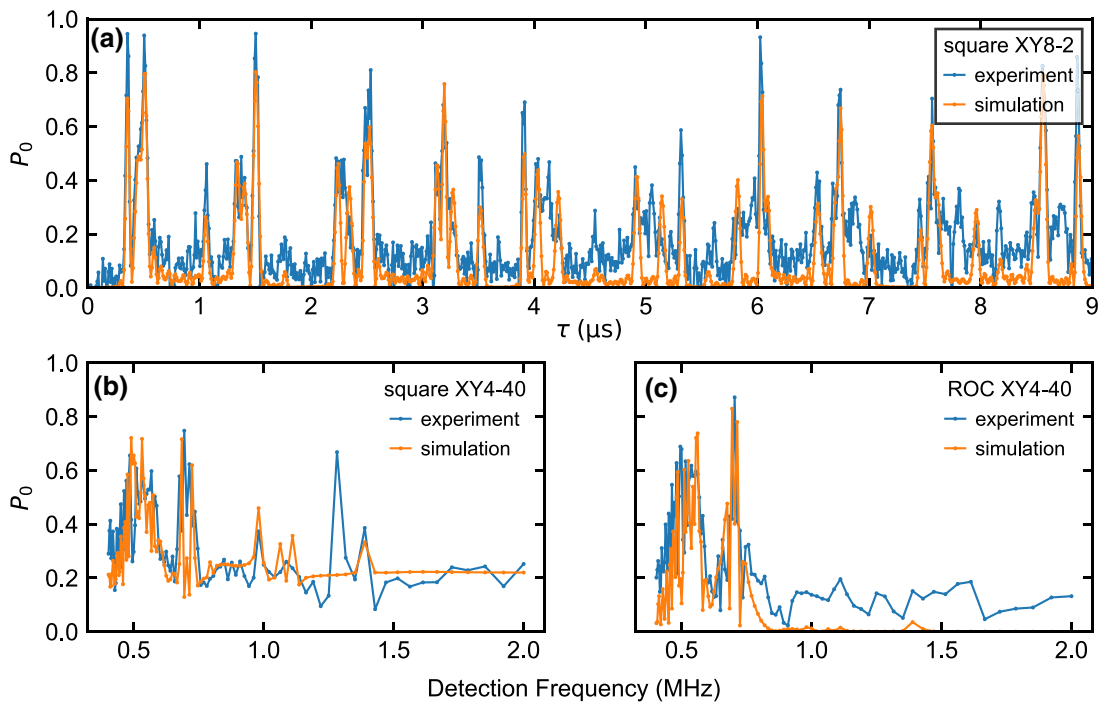


FIG. 5. (a) Experiment (blue line) and simulation (orange line) of detecting nuclear spins with XY8-2 sequence. The simulation is based on five ^{13}C nuclear spins coupled with a N-V center and their coupling strengths are shown in Table I. Experiments and simulations of detecting nuclear spins with XY4-40 sequences implemented with square (b) and ROC pulses (c) under an off-resonance condition. Both detunings and Rabi errors are set to $8\% \times \Omega$. The detection frequency is $f = 1/(4\tau)$. A spurious peak at 1.39 MHz resulting from the resonant peak at 0.69 MHz [shown in (b)], is suppressed by ROC-based DD sequences [shown in (c)].

imperfections, thus when interpulse delay satisfies $2\tau = k\pi/(2\omega_0)$, phase accumulation occurs during π pulses [26,27]. The phase accumulation at the second harmonic grows as the number of π pulses increases and introduces spurious peaks in the detected spectrum, which leads to difficulties in identifying resonance peaks. To avoid false identifications, substantial robust DD sequences have been proposed [28–32]. When the pulse imperfections are relatively large, our previous theoretical work [18] indicates that the performance of reported robust DD sequences can be further improved by combining with ROC pulses, resulting in a rather distinguishable spectrum.

Here, we first prepare a single N-V electron spin in a superposition $|x\rangle = 1/\sqrt{2}(|0\rangle - i|1\rangle)$ by applying a rotational operation about the x axis by an angle $\pi/2$. After applying the XY8 sequence [33] twice (with a basic unit in the form of $\tau - \pi_x - 2\tau - \pi_y - 2\tau - \pi_x - 2\tau - \pi_y - 2\tau - \pi_y - 2\tau - \pi_x - 2\tau - \pi_y - 2\tau - \pi_x - \tau$), another rotation about the x axis by an angle $\pi/2$ prepared the state to $|1\rangle$. The resulted population probability in $|1\rangle$ as a function of τ is shown in Fig. 5(a). According to the positions and depths of the harmonics, we find five ^{13}C coupled with the electron spin. Their coupling strengths and polar angles are summarized in Table I. In order to observe the spurious harmonics, we choose the XY4 sequence [33] (with a basic unit in the form of $\tau - \pi_x - 2\tau - \pi_y - 2\tau - \pi_x - \tau$)

$2\tau - \pi_y - \tau$) implemented with square and ROC under an off-resonance condition. Both MW detuning and Rabi error are set to be $8\% \times \Omega$. By repeating the sequence for 40 times, Fig. 5(b) shows a resonance peak at 0.695 MHz and a spurious peak at 1.39 MHz, which was induced by a strongly coupled nuclear spin (spin 1 in Table I) with its $a_{||} = 305$ kHz and $a_{\perp} = 136$ kHz. In comparison, by applying ROC algorithms in DD sequences, the background noise and spurious peaks caused by detunings and Rabi errors can be suppressed significantly, giving rise to a much more clear spectrum [Fig. 5(c)] revealing the electron-nuclear couplings.

TABLE I. Hyperfine coupling strengths ω_h and polar angles θ for four nuclear spins identified in Fig. 5. For each nuclear spin these values are obtained by individually fitting a single well isolated resonance.

Spin	$\omega_h/2\pi$ (kHz)	θ (degrees)
1	360(9)	56(2)
2	46(1)	178.3(5)
3	152(5)	134(2)
4	107(1)	122(1)
5	67(4)	26(1)

VI. CONCLUSION

Noise-resilient quantum gates devised by the robust optimal control algorithm are demonstrated experimentally with considerable improvement of gate fidelities. Unlike hard pulses, shaped pulses with smooth constraints are more friendly to hardware implementation. By generating quantum gates with ROC pulses, the errors introduced by MW detunings and fluctuations of MW powers can be suppressed. In addition, combining DD sequence with ROC pulses can suppress all spurious peaks to a satisfactory extent. Furthermore, our approach is fully compatible with other quantum systems, such as superconducting qubits, trapped ions, and Rydberg atoms. It would also be an intriguing technique capable of improving solid-state ensemble spin sensors, such as N-V centers in diamond, V_{Si} in SiC and organic spin sensors [34], of which the sensitivities are limited by inhomogeneous broadening [35] or dynamic biological environment [36].

ACKNOWLEDGMENTS

This study is supported by NSF of China (Grants No. 12004037, No. 91859121), Beijing Institute of Technology Research Fund Program for Young Scholars and the China Postdoctoral Science Foundation (Grant No. YJ20210035, No. 2021M700439). X.Y. and J.L. are supported by the National Natural Science Foundation of China (Grants No. 1212200199, No. 11975117, and No. 92065111), Guangdong Basic and Applied Basic Research Foundation (Grant No. 2021B1515020070), Guangdong Provincial Key Laboratory (Grant No. 2019B121203002), and Shenzhen Science and Technology Program (Grants No. RCYX20200714114522109 and No. KQTD20200820113010023). T.X. is supported by the China Postdoctoral Science Foundation (Grants No. 2021M703110, No. 2022T150631) and NSF of China (Grant No. 12274396).

APPENDIX A: OPTIMIZATION OF MW PULSES

In our experiments, manipulations of qubits are achieved by microwave pulses, which are generated by an arbitrary wave generator (AWG70001A, Tektronix), amplified with a power amplifier (ZHL-15W-422-S+, Mini Circuits) and applied through a coplanar waveguide (CPW). In order to minimize the effects induced by both the Overhauser field (caused by interactions with nuclear-spin-bath) and the distortion of microwave amplitudes (caused by limited bandwidth), we design and fabricate an ultrabroadband CPW structure with a bandwidth up to 6 GHz [37]. The scattering parameters of the CPW shown in Fig. 6 are measured by a microwave analyzer (N9917A, Keysight). We find that leakages and reflections between microwave components resulting in extra distortions of microwave pulses, which decreased the fidelity

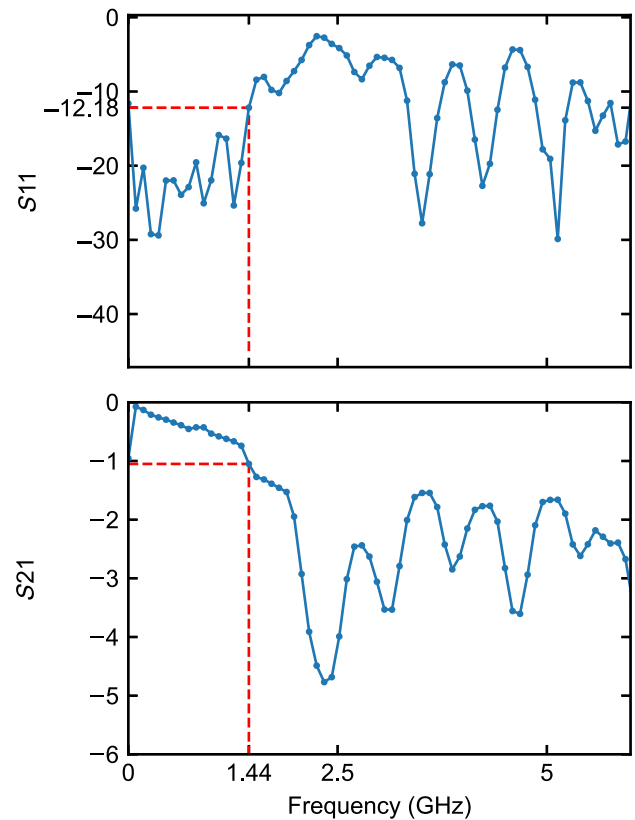


FIG. 6. Scattering parameters of the CPW. The S_{11} and S_{21} parameters at 1.44 GHz are -12.18 and -1.05 dB, respectively.

of quantum gates. Figure 7(a) shows the waveforms of square, CORPSE, and BB1. It is apparent that there are distortions at the beginning and the end of pulses. For composite pulses, there are additional distortions between each pulses. Additionally, noise and distortions of phase are found in these pulses [Fig. 7(b)]. In order to suppress the distortions and noises, we insert a 6-dB attenuator at the output port of the microwave source. And at the output port of the power amplifier, we insert attenuators and an isolator with its frequency bandwidth ranging from 1.42 to 1.54 GHz. Comparisons of the waveforms and phases obtained before and after the circuitry optimization are shown in Fig. 7. The amplitude distortions and phase noises are successfully reduced.

APPENDIX B: HIGH-FIDELITY QUANTUM GATE

We denote a single-qubit gate as $(\theta)_\phi$ corresponding to a rotation in the rotating frame of angle θ around the axis in the equatorial plane with azimuth ϕ . Waveforms of four types of $(\pi)_0$ gate are shown in Fig. 8(b). The CORPSE [16] is depicted as $(\theta_1)_0 - (\theta_2)_\pi - (\theta_3)_0$, with rotation angles $\theta_1 = 2\pi + \theta/2 - \arcsin(\sin(\theta/2)/2)$, $\theta_2 = 2\pi - 2 \arcsin(\sin(\theta/2)/2)$, and $\theta_3 = \theta/2 - \arcsin(\sin(\theta/2)/2)$. The pulse sequence of BB1 [38] is $(\theta/2)_0 - (\pi)_\phi - (2\pi)_{3\phi} - (\pi)_\phi - (\theta/2)_0$,

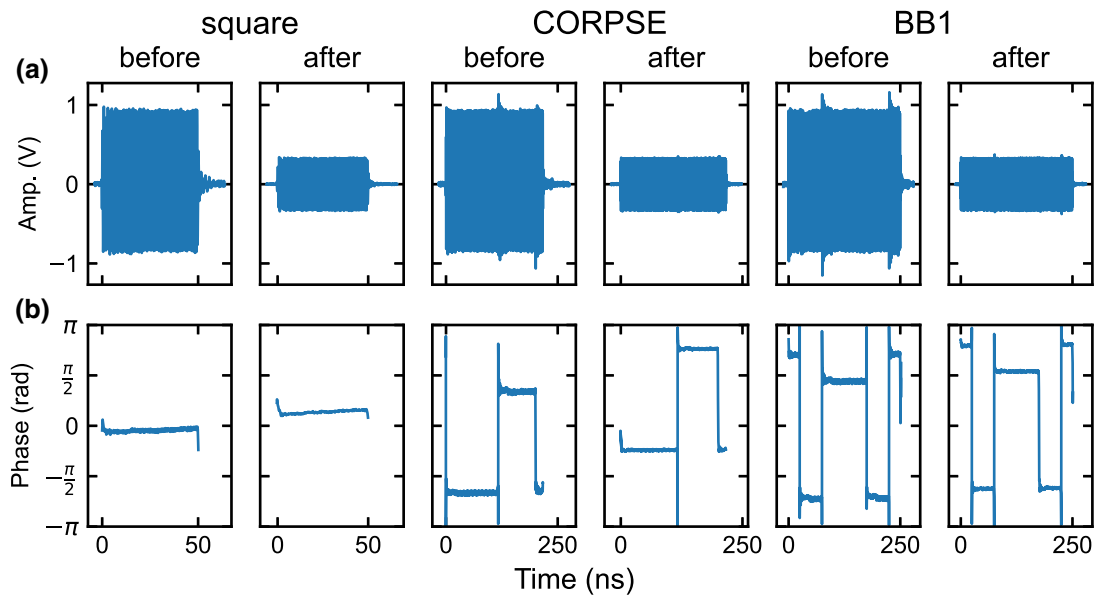


FIG. 7. Optimization of microwave pulses. (a) Waveforms of square, CORPSE, and BB1 before and after the optimization. (b) Results of phase demodulation before and after the optimization.

where $\phi = \arccos(-\theta/4\pi)$. ROC is generated by robust optimal control methods [18]. Its amplitude and phase varied with time. The in-phase components u_x and quadrature components u_y of the four types of pulses are shown in Fig. 8(a). A π pulse with an arbitrary phase angle ϕ can be described with $(u_x \cos \phi - u_y \sin \phi)\hat{S}_x + (u_x \sin \phi + u_y \cos \phi)\hat{S}_y$.

APPENDIX C: NORMALIZATION OF EXPERIMENTAL DATA

The general experiment schematic is shown in Fig. 9. The photon number obtained in the first counting event was recorded as I_{sig} , and the one obtained in the subsequent event is recorded as I_{ref} is the reference. The experimental data is calculated by $C = \bar{I}_{\text{sig}} - \bar{I}_{\text{ref}}/\bar{I}_{\text{ref}}$, where $\bar{I}_{\text{sig}}(\bar{I}_{\text{ref}})$

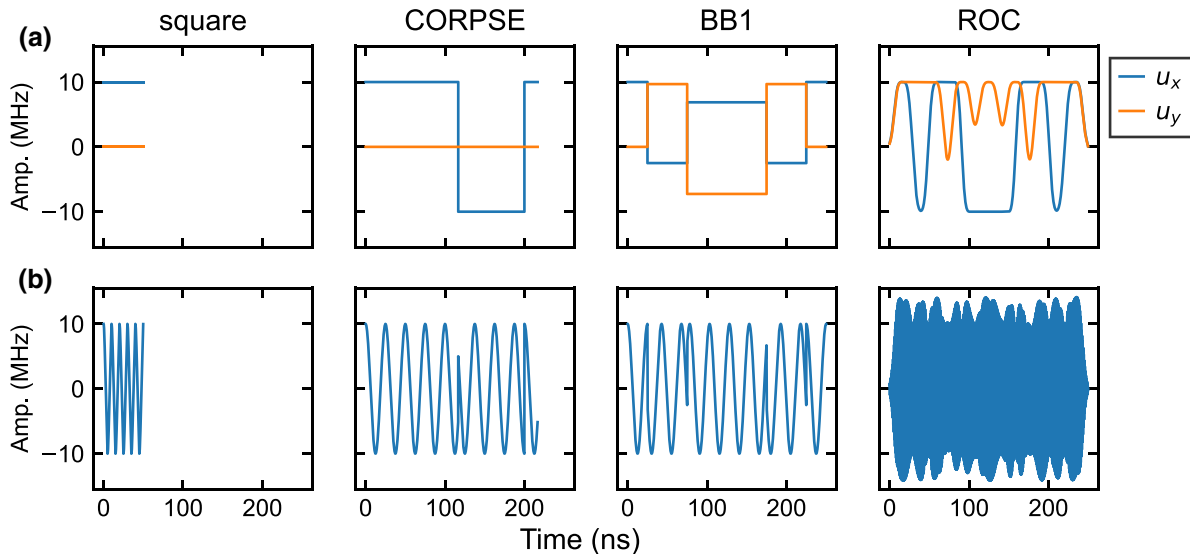


FIG. 8. (a) Amplitudes of in-phase components (blue lines) and quadrature components (yellow lines) of $(\pi)_0$ gates. (b) Waveform schematics of square, CORPSE, BB1, and ROC.

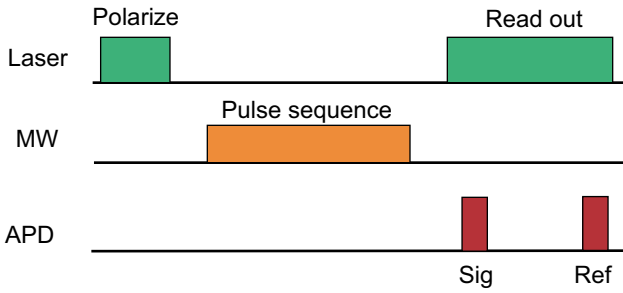


FIG. 9. General experimental procedure for high-fidelity quantum gates.

stands for the averaged value of I_{sig} (I_{ref}) collected in 8×10^5 datasets. The error for each experimental data can be derived according to

$$\Delta C = \frac{\Delta I_{\text{sig}} \cdot \bar{I}_{\text{ref}} + \Delta I_{\text{ref}} \cdot \bar{I}_{\text{sig}}}{\bar{I}_{\text{sig}}^2}, \quad (\text{C1})$$

where $\Delta \bar{I}_{\text{sig}}$ and $\Delta \bar{I}_{\text{ref}}$ denote standard deviations of \bar{I}_{sig} and \bar{I}_{ref} , respectively. In general, a quantum state tomography [39,40] is normally used to get fidelity of final state. However, in our experiments, final states are either $|m_s = 0\rangle$ or $|m_s = -1\rangle$, so we need only to obtain the diagonal elements of the density matrix. Normalization of the experimental data is carried out by performing Rabi experiments. By fitting the data obtained from Rabi experiments with a sinusoidal function, the population probability of $|m_s = 0\rangle$ is given by

$$P_{|m_s=0\rangle} = \frac{C - C_{\min}}{C_{\max} - C_{\min}}, \quad (\text{C2})$$

where C_{\min} and C_{\max} are the maximum and minimum values of the fitted curve.

APPENDIX D: ROBUST OPTIMAL CONTROL

The robust optimal control method that we adopt in our work is based on Ref. [18]. Here we plot a flow chart (see Fig. 10) to show the procedures of generating a ROC pulse. The procedures start from initializing some parameters including (1) the operator U_t to be optimized [here we take $U_t = (\pi)_0$]; (2) the pulse length L ; (3) two weights of noise, ϵ_1 for detunings and ϵ_2 for Rabi errors; (4) the maximum order of directional derivatives m_{\max} ; (5) a set of weights specifying the relevance of the associated objective function $\mu_{i_1, i_2}^{(m)}$. Then according to the results of evolution simulation, the fitness function is calculated by

$$\Phi(u) = |\text{Tr}(U_C(\tau_u)R_0^\dagger(\theta))|^2 - \sum_{m=1}^{m_{\max}} \sum_{i_1, i_2=1}^2 \mu_{i_1, i_2}^{(m)} \|\mathcal{D}_{U_C}^{(m)}(V_{i_1}, V_{i_2})\|^2. \quad (\text{D1})$$

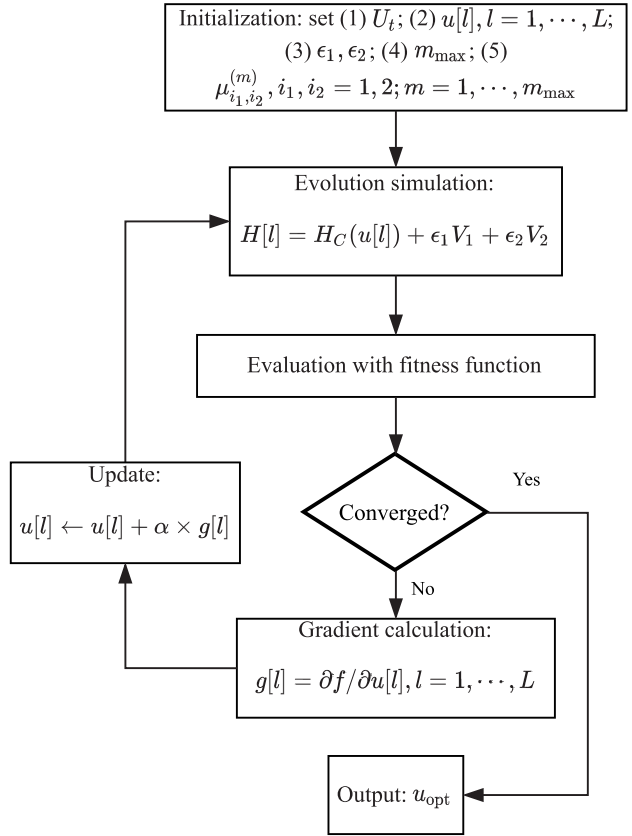


FIG. 10. Flow chart of generating pulses with the ROC method.

where $U_C(\tau_u)$ is the evolution operator of control filed at time τ_u , $R_0(\theta)$ is the ideal rotating operator, $\mathcal{D}_{U_C}^{(m)}(V_{i_1}, V_{i_2})$ is the m -order directional derivatives of U_C . If Φ is sufficiently high, the shaped pulse u is output, otherwise, the gradient of the fitness function with respect to the pulse parameters $g[l] = \partial \Phi / \partial u[l]$ is computed. By determining an appropriate step length α along the search direction $g[l]$, we update the pulse parameters $u[l] \leftarrow u[l] + \alpha \times g[l]$ and go back to the simulation step.

APPENDIX E: RANDOMIZED BENCHMARKING

The RB method [20] consists of a large number of experiments. Each experiment includes the preparation of an initial state $|m_s = 0\rangle$, application of a sequence containing $m + 1$ random Clifford gates, and measuring final states. Each Clifford gate, except the last one, is chosen randomly from the Clifford group, which contains 24 rotations preserving the octahedron in the Bloch sphere [20]. Each rotation can be decomposed into rotations around the X and Y axes, as summarized in Table II. The last Clifford gate is chosen to ensure the final state is a ground state. The average Clifford gate fidelity is achieved by

$$F_{\text{seq}} = A * p^m + B, \quad (\text{E1})$$

TABLE II. 24 Clifford gate representing with basic rotations. Here, X and X/2 denote a π and $\pi/2$ rotation around the X axis respectively. And I is an identity operator.

Paulies	I		
	X		
	Y		
	X,	Y	
2 $\pi/3$ rotations	X/2, X/2, -X/2, -X/2, Y/2, Y/2, -Y/2, -Y/2,	Y/2 -Y/2 Y/2 -Y/2 X/2 -X/2 X/2 -X/2	
$\pi/2$ rotations	X/2 -X/2 Y/2 -Y/2 -X/2, -X/2, X, X, Y, Y, X/2, -X/2,	Y/2, -Y/2 X/2 -X/2 Y/2, -Y/2 Y/2 -Y/2 X/2 -X/2	X/2
Hadamard-like			

where F_{seq} is the resulting sequence fidelity obtained by averaging k different sequences. p is the sequence decay, and state preparation and measurement errors are captured in the parameters A and B . The average fidelity per Clifford gate is $F_c = 1 - (1 - p)/2$. Equation (E1) can be simplified via a detuning experiment. The experiment concept is shown in Fig. 11. We polarize an electron spin to the ground state, a RB sequence whose frequency had a $2\pi \times 2$ GHz detuning from resonance was applied. After reading states population and repolarizing the spin, a blank sequence, whose duration equal to that of the first RB sequence, is inserted before readout of reference to exclude the effects of longitudinal relaxation. Thus the final sequence fidelity decreases only due to errors of state

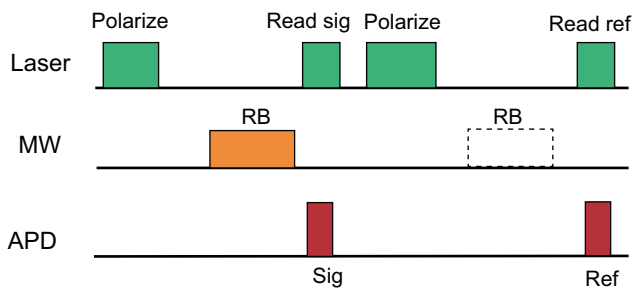


FIG. 11. Concept and experimental procedures of detuning experiment for randomized benchmarking.

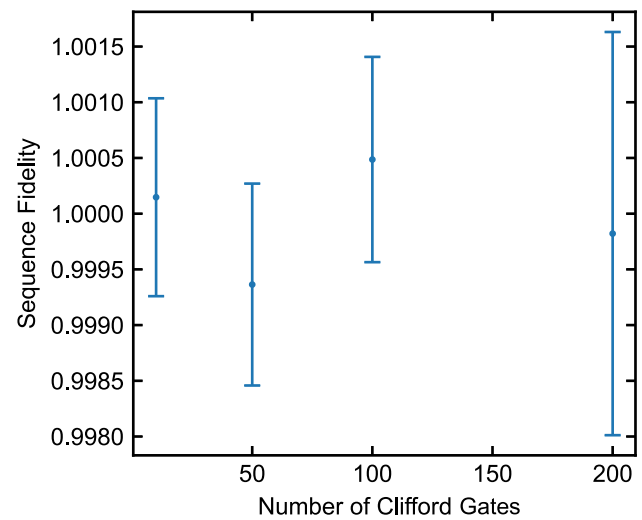


FIG. 12. Experimental result of detuning experiment. The number of samples to be averaged is set to be 100. Error bars on the figure is the standard deviation from the mean.

polarization and measurements. The experimental result is shown in Fig. 12 and we find the sequence fidelity did not decrease even when the number of Clifford gates is set to be 200. Thus we simplify Eq. (E1) into

$$F_{\text{seq}} = \frac{1}{2}p^m + \frac{1}{2}. \quad (\text{E2})$$

- [1] Y. Chou, S.-Y. Huang, and H.-S. Goan, Optimal control of fast and high-fidelity quantum gates with electron and nuclear spins of a nitrogen-vacancy center in diamond, *Phys. Rev. A* **91**, 052315 (2015).
- [2] N. Khaneja, T. Reiss, C. Kehlet, T. Schulte-Herbrüggen, and S. J. Glaser, Optimal control of coupled spin dynamics: design of NMR pulse sequences by gradient ascent algorithms, *J. Magn. Reson.* **172**, 296 (2005).
- [3] E. Van Reeth, H. Ratiney, M. Lapert, S. J. Glaser, and D. Sugny, Optimal control theory for applications in magnetic resonance imaging, *Pac. J. Math.* **9**, 9 (2017).
- [4] G. Fuchs, G. Burkard, P. Klimov, and D. Awschalom, A quantum memory intrinsic to single nitrogen–vacancy centres in diamond, *Nat. Phys.* **7**, 789 (2011).
- [5] G. Waldherr, Y. Wang, S. Zaiser, M. Jamali, T. Schulte-Herbrüggen, H. Abe, T. Ohshima, J. Isoya, J. Du, and P. Neumann, *et al.*, Quantum error correction in a solid-state hybrid spin register, *Nature* **506**, 204 (2014).
- [6] P. Neumann, R. Kolesov, B. Naydenov, J. Beck, F. Rempp, M. Steiner, V. Jacques, G. Balasubramanian, M. Markham, and D. Twitchen, *et al.*, Quantum register based on coupled electron spins in a room-temperature solid, *Nat. Phys.* **6**, 249 (2010).
- [7] T. Häberle, D. Schmid-Lorch, K. Karrai, F. Reinhard, and J. Wrachtrup, High-Dynamic-Range Imaging of Nanoscale

- Magnetic Fields Using Optimal Control of a Single Qubit, *Phys. Rev. Lett.* **111**, 170801 (2013).
- [8] F. Shi, X. Kong, P. Wang, F. Kong, N. Zhao, R.-B. Liu, and J. Du, Sensing and atomic-scale structure analysis of single nuclear-spin clusters in diamond, *Nat. Phys.* **10**, 21 (2014).
- [9] F. Shi, Q. Zhang, P. Wang, H. Sun, J. Wang, X. Rong, M. Chen, C. Ju, F. Reinhard, and H. Chen, *et al.*, Single-protein spin resonance spectroscopy under ambient conditions, *Science* **347**, 1135 (2015).
- [10] N. Aslam, M. Pfender, P. Neumann, R. Reuter, A. Zappe, F. F. De Oliveira, A. Denisenko, H. Sumiya, S. Onoda, and J. Isoya, *et al.*, Nanoscale nuclear magnetic resonance with chemical resolution, *Science* **357**, 67 (2017).
- [11] J. Cerrillo, S. Oviedo Casado, and J. Prior, Low Field Nano-NMR via Three-Level System Control, *Phys. Rev. Lett.* **126**, 220402 (2021).
- [12] V. V. Soshenko, S. V. Bolshedvorskii, O. Rubinas, V. N. Sorokin, A. N. Smolyaninov, V. V. Vorobyov, and A. V. Akimov, Nuclear Spin Gyroscope Based on the Nitrogen Vacancy Center in Diamond, *Phys. Rev. Lett.* **126**, 197702 (2021).
- [13] P. Rembold, N. Oshnik, M. M. Müller, S. Montangero, T. Calarco, and E. Neu, Introduction to quantum optimal control for quantum sensing with nitrogen-vacancy centers in diamond, *AVS Quantum Sci.* **2**, 024701 (2020).
- [14] M. H. Levitt, Composite pulses, *Prog. Nucl. Magn. Reson. Spectrosc.* **18**, 61 (1986).
- [15] S. Wimperis, Broadband, narrowband, and passband composite pulses for use in advanced NMR experiments, *J. Magn. Reson.* **109**, 221 (1994).
- [16] H. K. Cummins, G. Llewellyn, and J. A. Jones, Tackling systematic errors in quantum logic gates with composite rotations, *Phys. Rev. A* **67**, 042308 (2003).
- [17] X. Rong, J. Geng, F. Shi, Y. Liu, K. Xu, W. Ma, F. Kong, Z. Jiang, Y. Wu, and J. Du, Experimental fault-tolerant universal quantum gates with solid-state spins under ambient conditions, *Nat. Commun.* **6**, 8748 (2015).
- [18] X. Yang, Y. Ge, B. Zhang, and J. Li, Robust dynamical decoupling for the manipulation of a spin network via a single spin, (2021), arXiv preprint [ArXiv:2101.03976](https://arxiv.org/abs/2101.03976).
- [19] H. Haas, D. Puzzuoli, F. Zhang, and D. G. Cory, Engineering effective hamiltonians, *New J. Phys.* **21**, 103011 (2019).
- [20] R. Barends, *et al.*, Superconducting quantum circuits at the surface code threshold for fault tolerance, *Nature* **508**, 500 (2014).
- [21] E. Magesan, J. M. Gambetta, and J. Emerson, Scalable and Robust Randomized Benchmarking of Quantum Processes, *Phys. Rev. Lett.* **106**, 180504 (2011).
- [22] E. Magesan, J. M. Gambetta, B. R. Johnson, C. A. Ryan, J. M. Chow, S. T. Merkel, M. P. da Silva, G. A. Keefe, M. B. Rothwell, T. A. Ohki, M. B. Ketchen, and M. Steffen, Efficient Measurement of Quantum Gate Error by Interleaved Randomized Benchmarking, *Phys. Rev. Lett.* **109**, 080505 (2012).
- [23] T. D. Ladd, F. Jelezko, R. Laflamme, Y. Nakamura, C. Monroe, and J. L. O'Brien, Quantum computers, *Nature* **464**, 45 (2010).
- [24] C. E. Bradley, J. Randall, M. H. Abobeih, R. C. Berrevoets, M. J. Degen, M. A. Bakker, M. Markham, D. J. Twitchen, and T. H. Taminiau, A Ten-Qubit Solid-State Spin Register with Quantum Memory up to One Minute, *Phys. Rev. X* **9**, 031045 (2019).
- [25] T. H. Taminiau, J. J. T. Wagenaar, T. van der Sar, F. Jelezko, V. V. Dobrovitski, and R. Hanson, Detection and Control of Individual Nuclear Spins Using a Weakly Coupled Electron Spin, *Phys. Rev. Lett.* **109**, 137602 (2012).
- [26] M. Loretz, J. M. Boss, T. Rosskopf, H. J. Mamin, D. Rugar, and C. L. Degen, Spurious Harmonic Response of Multi-pulse Quantum Sensing Sequences, *Phys. Rev. X* **5**, 021009 (2015).
- [27] S. Pasini, P. Karbach, and G. S. Uhrig, High-order coherent control sequences of finite-width pulses, *Europhys. Lett.* **96**, 10003 (2011).
- [28] G. T. Genov, D. Schraft, N. V. Vitanov, and T. Halfmann, Arbitrarily Accurate Pulse Sequences for Robust Dynamical Decoupling, *Phys. Rev. Lett.* **118**, 133202 (2017).
- [29] A. M. Souza, G. A. Álvarez, and D. Suter, Robust Dynamical Decoupling for Quantum Computing and Quantum Memory, *Phys. Rev. Lett.* **106**, 240501 (2011).
- [30] Z.-Y. Wang, J. E. Lang, S. Schmitt, J. Lang, J. Casanova, L. McGuinness, T. S. Monteiro, F. Jelezko, and M. B. Plenio, Randomization of Pulse Phases for Unambiguous and Robust Quantum Sensing, *Phys. Rev. Lett.* **122**, 200403 (2019).
- [31] J. Casanova, Z.-Y. Wang, J. F. Haase, and M. B. Plenio, Robust dynamical decoupling sequences for individual-nuclear-spin addressing, *Phys. Rev. A* **92**, 042304 (2015).
- [32] J. Casanova, Z.-Y. Wang, and M. B. Plenio, Noise-Resilient Quantum Computing with a Nitrogen-Vacancy Center and Nuclear Spins, *Phys. Rev. Lett.* **117**, 130502 (2016).
- [33] T. Gullion, D. B. Baker, and M. S. Conradi, New, compensated Carr-Purcell sequences, *J. Magn. Reson. (1969-1992)* **89**, 479 (1990).
- [34] H. Wu, S. Yang, M. Oxborrow, M. Jiang, Q. Zhao, D. Budker, B. Zhang, and J. Du, Enhanced quantum sensing with room-temperature solid-state masers, *Sci. Adv.* **8**, eade1613 (2022).
- [35] T. Nöbauer, A. Angerer, B. Bartels, M. Trupke, S. Rotter, J. Schmiedmayer, F. Mintert, and J. Majer, Smooth Optimal Quantum Control for Robust Solid-State Spin Magnetometry, *Phys. Rev. Lett.* **115**, 190801 (2015).
- [36] P. Konzelmann, T. Rendler, V. Bergholm, A. Zappe, V. Pfannenstill, M. Garsi, F. Ziem, M. Niethammer, M. Widmann, and S.-Y. Lee, *et al.*, Robust and efficient quantum optimal control of spin probes in a complex (biological) environment: towards sensing of fast temperature fluctuations, *New J. Phys.* **20**, 123013 (2018).
- [37] W. Jia, Z. Shi, X. Qin, X. Rong, and J. Du, Ultra-broadband coplanar waveguide for optically detected magnetic resonance of nitrogen-vacancy centers in diamond, *Rev. Sci. Instrum.* **89**, 064705 (2018).
- [38] S. Wimperis, Broadband, narrowband, and passband composite pulses for use in advanced NMR experiments, *J. Magn. Reson., Ser. A* **109**, 221 (1994).
- [39] A. M. Childs, I. L. Chuang, and D. W. Leung, Realization of quantum process tomography in NMR, *Phys. Rev. A* **64**, 012314 (2001).
- [40] G. M. Leskowitz, and L. J. Mueller, State interrogation in nuclear magnetic resonance quantum-information processing, *Phys. Rev. A* **69**, 052302 (2004).